Title

Intracranial brain stimulation modulates fMRI-based network switching

Authors

Mangor Pedersen [1,2*] & Andrew Zalesky [3,4].

Affiliations

1. Department of Psychology and Neuroscience, Auckland University of Technology (AUT), Auckland, New Zealand

2. The Florey Institute of Neuroscience and Mental Health, The University of Melbourne, Melbourne, VIC, Australia.

3. Department of Psychiatry, Melbourne Neuropsychiatry Centre, The University of Melbourne, VIC, Australia.

4. Melbourne School of Engineering, The University of Melbourne, VIC, Australia.

*** Corresponding author:** School of Clinical Sciences, Auckland University of Technology (AUT), Private Bag 92006, Victoria St West, New Zealand. E-mail: mangor.pedersen@aut.ac.nz

Manuscript information:

Character count manuscript: 41451 characters incl. spaces

Word count abstract: 222

Figures: 6

Number of references: 90

Supplemental information: 10

Summary

The extent to which resting-state fMRI (rsfMRI) reflects direct neuronal changes remains unknown. Using 160 simultaneous rsfMRI and intracranial brain stimulation recordings acquired in 26 individuals with epilepsy (with varying electrode locations), we tested whether brain networks dynamically change during intracranial brain stimulation, aiming to establish whether switching between brain networks is reduced during intracranial brain stimulation. As the brain spontaneously switches between a repertoire of intrinsic functional network configurations and the rate of switching is typically increased in brain disorders, we hypothesised that intracranial stimulation would reduce the brain's switching rate, thus potentially normalising aberrant brain network dynamics. To test this hypothesis, we quantified the rate that brain regions changed networks over time in response to brain stimulation, using *network switching* applied to multilayer modularity analysis of time-resolved rsfMRI connectivity. Network switching was significantly decreased during epochs with brain stimulation compared to epochs with no brain stimulation. The initial stimulation onset of brain stimulation was associated with the greatest decrease in network switching, followed by a more consistent reduction in network switching throughout the scans. These changes were most commonly observed in cortical networks spatially distant from the stimulation targets. Our results suggest that neuronal perturbation is likely to modulate large-scale brain networks, and multilayer network modelling may be used to inform the clinical efficacy of brain stimulation in neurological disease.

Highlights

- rsfMRI network switching is attenuated during intracranial brain stimulation
- Stimulation-induced switching is observed distant from electrode targets
- Our results are validated across a range of network parameters
- Network models may inform clinical efficacy of brain stimulation

Keywords

Multilayer networks, fMRI, network switching, intracranial brain stimulation, epilepsy.

Introduction

Network modularity encompasses a family of algorithms that quantify whether a collection of network nodes exert stronger 'intramodular' connectivity than expected by chance – i.e., modularity provides a set of subnetworks with stronger than average within-network connectivity (Sporns and Betzel, 2016). Multilayer network modularity represents a multidimensional version of network modularity (De Domenico, 2017; Mucha et al., 2010). A multilayer network is conceptualised as a 'network of networks' that are connected across several dimensions (Bassett et al., 2013; Betzel and Bassett, 2017; Vaiana and Muldoon, 2018). This is an explicit modelling framework that allows information to be shared across edges connected, for example in space and time, enabling us to track *where* and *when* entities in a network transit between different sub-networks or modules. In turn, spatiotemporal network measures like multilayer modularity are promising approaches that can enhance our understanding of human brain function, and a way to monitor the clinical response to invasive treatment strategies, including intracranial brain stimulation.

By extending the concept of modularity to several dimensions, rsfMRI connectivity can be represented in terms of a spatiotemporal network model of the brain (Finc et al., 2020; Lydon-Staley et al., 2018; Shine et al., 2016). Multilayer network flexibility, or switching, is associated with cognitive functions including working memory (Braun et al., 2015), reasoning (Pedersen et al., 2018a), reward (Gerraty et al., 2018) and fatigue (Betzel et al., 2017) as well as alterations in multiple psychological and neurological disorders (Gifford et al., 2020; Harlalka et al., 2019; Long et al., 2019; Paban et al., 2019; Shao et al., 2019; Tian et al., 2020a). There is also evidence that brain network switching changes in response to behavioural training. For example, Bassett et al. (2011) showed that motor training is associated with greater network switching, particularly in association cortices involved in higher-order cognition. A follow-up study demonstrated that brain network switching on the first day of motor training was correlated with individual differences in overall motor learning rate (Telesford et al., 2017). Another study showed increased brain network switching in people who underwent half-a-year of musical training, compared to people with no musical training (Li et al., 2019). These studies suggest cause-and-effect relationships such as overt learning (e.g., motor, and musical training) can alter the brain's network switching rate.

It remains unknown whether focal neuronal perturbation –for example via invasive brain stimulation– leads to observable changes in the rate at which the brain switches between rsfMRI networks. In this study, we used the above-mentioned multilayer modularity model (Mucha et al., 2010) to investigate spatiotemporal network changes that occur during short periods of intermittent brain stimulation. Such spatiotemporal network models are advantageous for this purpose as they can pinpoint the

specific time-points when brain regions transit between networks. Elucidating network switching during brain stimulation will provide new insights into the dynamical properties of rsfMRI networks.

To test whether brain network switching is altered during intracranial brain stimulation, we used rsfMRI data with concurrent intracranial stimulation acquired from individuals with treatment-resistant focal epilepsy and uncontrollable seizures. Focal epilepsy is a neurological disease associated with increased rsfMRI connectivity (Bernhardt et al., 2011, 2015; Hong et al., 2017; Pedersen et al., 2015, 2016, 2017), and prior electrophysiology research in epilepsy suggests that the impact of brain stimulation results in changes to neuronal networks and provides clinical benefits likely by 'steering' the brain into a temporary state associated with modulated network events (Li and Yang, 2017). We hypothesise that stimulation-induced network changes can also be observed at the macroscale with advanced rsfMRI methods. As high-frequency stimulation (here, 100 Hz) is commonly thought to be associated with neuronal inhibition (see Garcia et al. 2005, for a review), our directed hypothesis was that rsfMRI network switching significantly decreases during epochs with brain stimulation (*Stim*) compared to epochs with no brain stimulation (*NoStim*), in people with epilepsy.

Results

We studied 26 patients with treatment-resistant epilepsy for whom 160 rsfMRI scans were acquired while simultaneously receiving 100Hz intracranial electrical stimulation (Figure S1 – see also Oya et al., 2017 and Thompson et al., 2020). Intracranial brain stimulation is a common part of the pre-surgical work-up in treatment-resistant focal epilepsy patients. This is a useful way to detect surgical brain targets in epilepsy and it is known to reduce seizure frequency in focal epilepsy (Gummadavelli et al., 2015; Khan et al., 2009; Schulze-Bonhage, 2017; Toprani and Durand, 2013; Zangiabadi et al., 2019). Most participants had seizures originating from the mesial temporal lobes. The most common stimulation target was the amygdala followed by the Heschl's gyrus and the frontal/cingulate gyri. For the most part, participants were implanted with multiple electrodes, as shown in Figure 1.

As shown in Figure 2, a rsfMRI block design was used in this study with alternating 30 seconds NoStim epochs followed by 30-second Stim epochs. To quantify time-varying fMRI connectivity within relatively short half-a-minute epochs, we used instantaneous phase synchrony. Instantaneous phase synchrony quantifies narrow-band fMRI connectivity by estimating the phase difference between brain regions, at a single time-point resolution (Glerean et al., 2012; Pedersen et al., 2018b; Ponce-Alvarez et al., 2015). We used instantaneous phase synchrony as an input to an ordinal multilayer modularity network model, enabling us to quantify the percentage of times each brain region changes network allegiance –*i.e., network switching*– during intracranial brain stimulation.

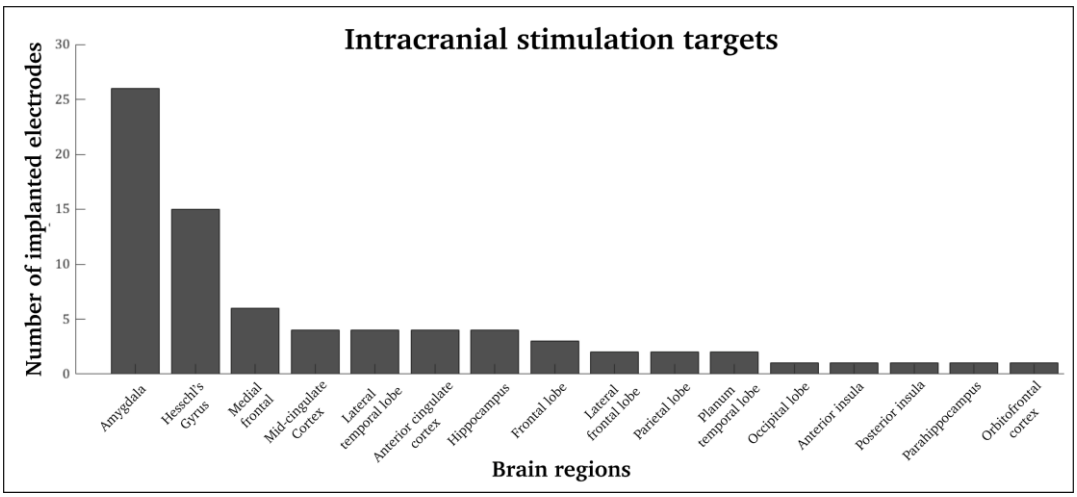

Figure 1: Location of brain electrodes across 26 epilepsy patients: *The most common stimulation site included the amygdala (26 electrodes) followed by Heschl's gyrus (15 electrodes) and the frontal/cingulate cortex. Note that most individuals were implanted with more than one electrode.*

We used a brain parcellation atlas that included 196 brain regions, to test our main hypothesis that brain network switching is reduced during brain stimulation (i.e., Stim), compared to periods with no brain stimulation (i.e., NoStim). This parcellation mask was created by combining a parcellation atlas from the Human Connectome Project that included 180 cortical brain regions (Glasser et al., 2016) and a parcellation atlas from Tian et al., (2020b) that includes 16 subcortical brain regions (Figure S2). We conducted our analyses using symmetric homologous brain regions, to counter laterality effects of focal epilepsy, as patients have seizures that originate from a single hemisphere (Adcock et al., 2003). For each rsfMRI scan, we obtained a regions × regions × time connectivity tensor (196 × 196 × 160). We included 80 Stim and 80 NoStim time-points (10 time-points per 30-second epoch with a rsfMRI repetition time of 3 seconds), to ensure that all rsfMRI scans contain the same number of time-points.

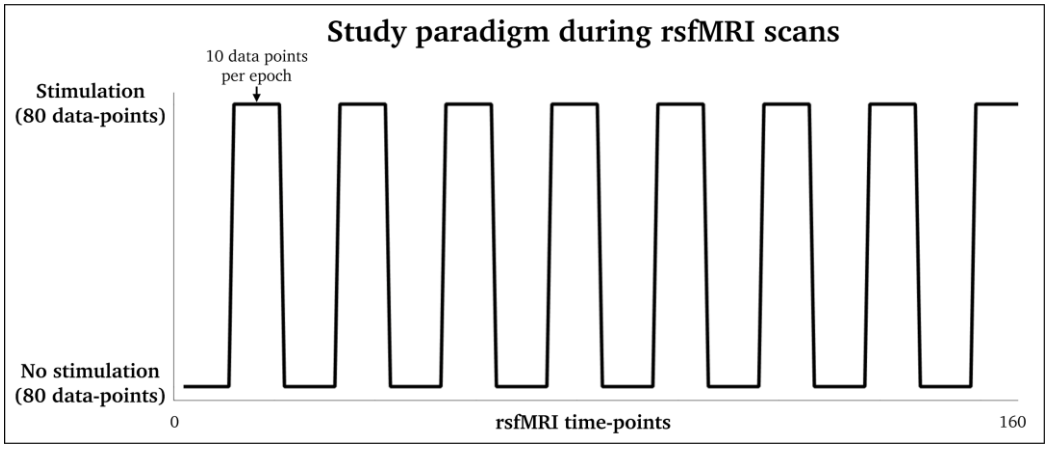

Figure 2: Study paradigm used during rsfMRI scans: *rsfMRI scans had 10 data-points with NoStim (30 seconds) followed by 10 data points of Stim (30 seconds), repeated eight times (16 epochs in total). This resulted in 80 Stim data points (4.5 minutes) and 80 NoStim data points (4.5 minutes), for each rsfMRI scan.*

We report findings based on thresholded/binarized instantaneous phase synchrony tensors at a 15% network density (i.e., retaining the top-15% synchronous connection-pairs, and a topological/temporal modularity resolution of γ/ω = 1, consistent with previous studies (Bassett et al., 2013). Replication analyses for multiple network densities (van den Heuvel et al., 2017; Langer et al., 2013) and multiple recommended γ/ω parameters (Yang et al., 2020) are also reported.

Group-level network switching is decreased during brain stimulation

As hypothesised, we observed significantly decreased network switching during Stim epochs compared to NoStim epochs, averaged across all brain regions (paired t-test: $t(159) = 5.8$, $p < 0.001$; based on an average of all Stim/NoStim epochs – see Figure 3A). A one-way repeated measures ANOVA demonstrated a significant main effect of network switching between all possible epochs, $F(15,2385) = 22.97$, $p < 0.001$. Post-hoc tests showed that 45% (54/120) of epoch combinations were statistically significant ($p < 0.05$, Bonferroni correction – see Figure 3B and Figure S4, for all statistical comparisons). The greatest reduction in network switching occurred after the first stimulation epoch (Figure 3A – left). The initial stimulation may 'startle' the brain as these epilepsy patients did not receive stimulation less than 1.5 hours (and up to 3 hours) before the rsfMRI acquisition. In subsequent epochs, network switching stabilized but continued to significantly decrease throughout the rsfMRI epochs. This implies a lasting network effect beyond the initial impact of brain stimulation and may reflect a long-lasting inhibition of local neuronal activity (Lafreniere-Roula et al., 2010).

We employed a temporal null model previously described by Bassett et al. (2013) to test whether the stimulation-induced changes in network switching could be explained by random dynamical processes. In this temporal null model, we randomly permuted rsfMRI time-points 100 times per rsfMRI scan before computing 100 'temporally random' multilayer modularity models per rsfMRI scan. This procedure preserves the topological modularity of networks but changes their temporal order. As seen in Figure 3B, we observed no differences between epochs when randomly permuting rsfMRI time-points (repeated measures ANOVA ($F(15,2385) = 0.1$, $p = 1$). The network switching was approximately six times greater in the temporal null model (Figure 3C), compared to the original data (Figure 3A). This finding suggests that temporal fluctuations of network switching in response to brain stimulation are unlikely to occur by chance.

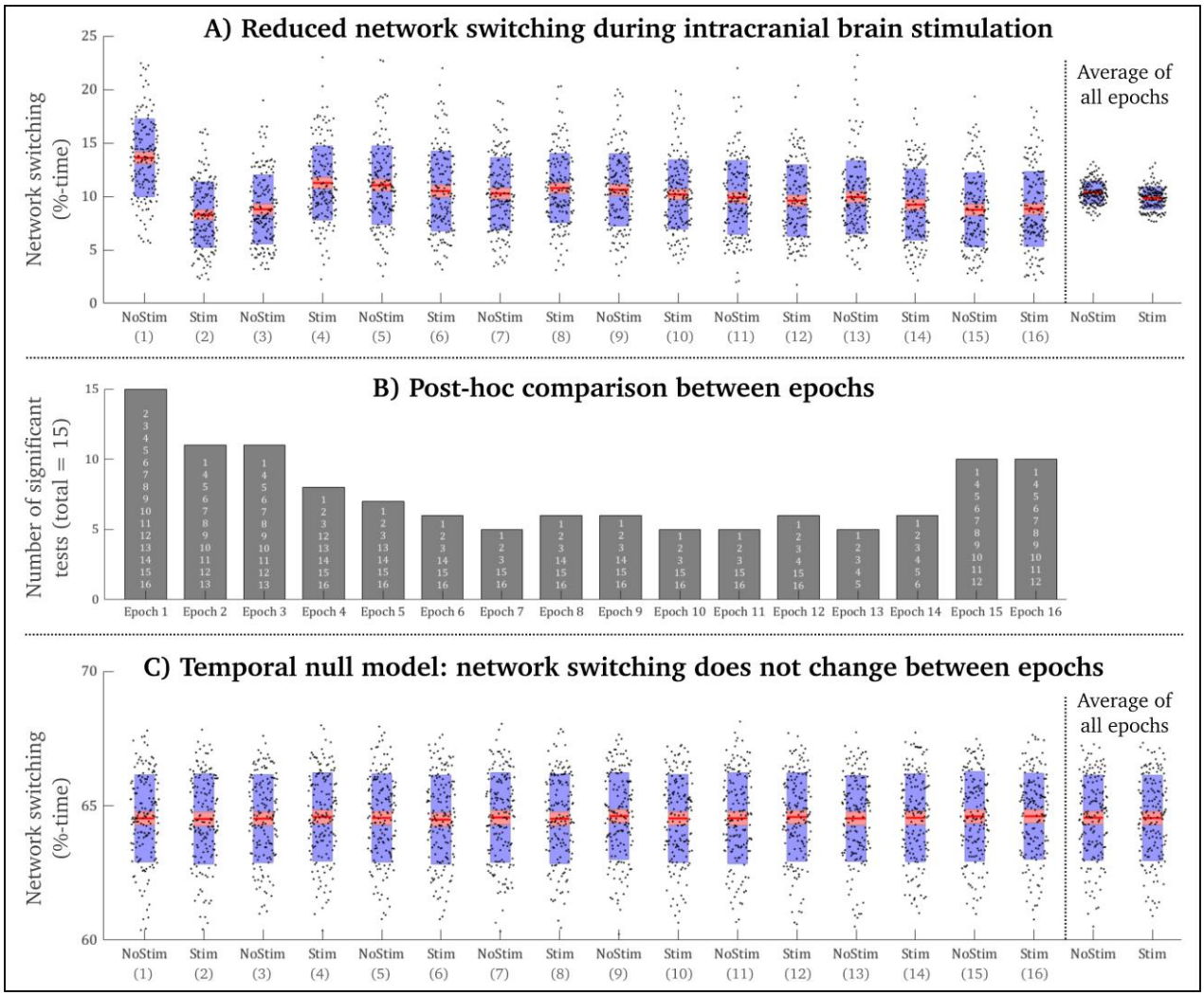

Figure 3: Stimulation-induced changes in network switching at group level: *A) Network switching shown as a function of time throughout the rsfMRI scans, stratified according to NoStim and Stim epochs (epoch numbers in parentheses). Here, network switching is the proportion of time that nodes switch network allegiance during Stim and NoStim epochs. The shaded red area is the 95th confidence interval of the mean. The shaded blue area is one standard deviation of the mean. B) An overview of post-hoc comparisons between all epochs. The white numbers inside the bars refer to the epoch numbers that are statistically significant for a reduction in network switching within the current epoch (Bonferroni corrected). C) Same as A, but here the rsfMRI time-points are randomly permuted 100 times before computing the multilayer modularity model – i.e., a temporal null model. We report the mean of the 100 permutations.*

Individual-level network switching is decreased during brain stimulation

Next, we tested the consistency of the above group-average results for each rsfMRI scan and individual. To do so, we computed the gradients *–i.e., the direction of temporal brain changes–* of network switching from NoStim to Stim epochs and vice versa, for each rsfMRI scan. Consistent with the group-average results, a negative gradient during the initial transition from NoStim to Stim (decreased network switching) was evident for 85% (136/160) of rsfMRI scans. There also appeared to be a 'rebound' effect between the third and fifth epoch, where the gradients are positive for most individuals (increased network switching). Subsequent transitions appear to show a balance between positive and negative gradients (Fig. 4). This suggests that network effects from the initial stimulation may be detected at both the group and individual level.

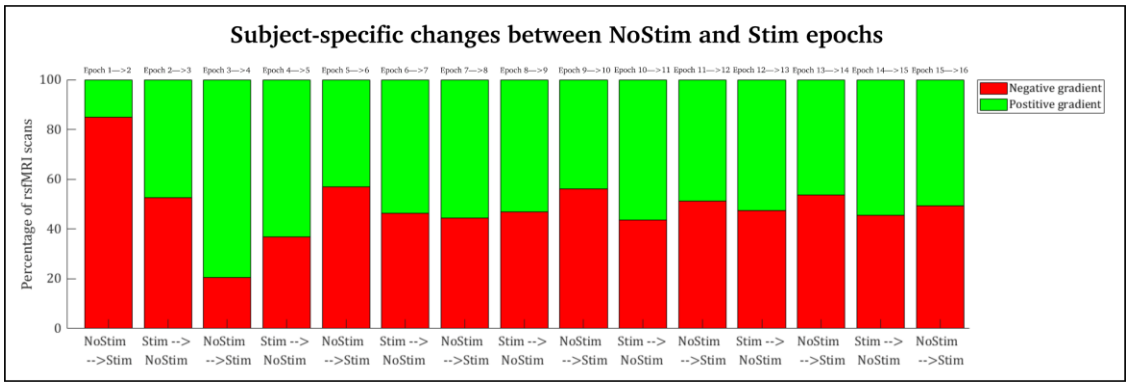

Figure 4: Individual changes in network switching during brain stimulation*: The percentage of rsfMRI scans with a negative and positive gradient of network switching are shown in blue and green, respectively. Gradients are computed between successive Stim and NoStim epochs. Negative gradients indicate a decrease in network switching induced by stimulation, while positive gradients indicate an increase.*

Specific brain regions display decreased network switching during brain stimulation

After establishing that brain-averaged network switching is reduced during brain stimulation, we aimed to delineate brain regions where this reduction was most prominent. We conducted a paired t-test for each of the 196 brain regions, between Stim and NoStim epochs (average of all NoStim and Stim epochs). Following False Discovery (FDR) correction for the 196 tests (Benjamini and Hochberg, 1995), the frontal cortex, parietal cortex, and temporal cortex displayed the strongest reduction in network switching during brain stimulation (Figure 5A and Figure S4).

Notably, significant differences in network switching between NoStim and Stim epochs were localized to regions distant from the most common stimulation sites, particularly the amygdala. Only 39% of statistically significant brain regions overlapped with intracranial electrodes, suggesting that brain stimulation may influence brain networks beyond the focal stimulation targets (Figure 5B).

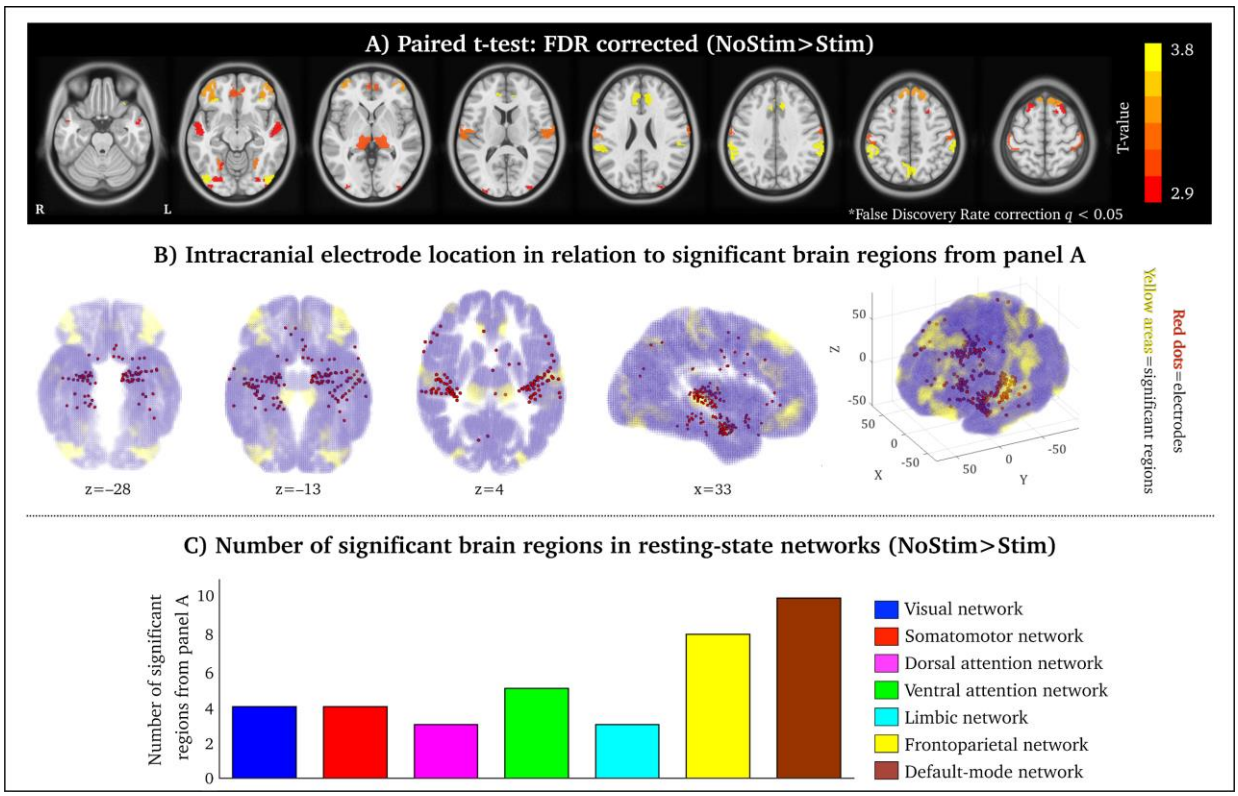

Figure 5: Regional changes in network switching between NoStim and Stim epochs: *A) Cortical and subcortical regions with a significant decrease in stimulation-induced network switching (paired t-test between Stim and NoStim, FDR corrected at q<0.05). B) Same as A, but here used to highlight the spatial proximity between intracranial electrodes and statistically significant brain regions, in 2D and 3D planes (NoStim<Stim). Electrodes are highlighted with red dots and significant brain regions are highlighted in yellow. 3/26 individuals in this study did not have coordinates for the intracranial electrodes. C) The number of significant brain regions within each of the seven resting-state networks (Yeo et al., 2011).*

Specific brain networks display decreased network switching during brain stimulation

To test the network-specific effect of stimulation-induced brain switching, we summarised the number of statistically significant brain regions (NoStim<Stim) residing in seven previously validated 'resting-state networks' (Yeo et al., 2011). The two brain networks with the most significant brain regions between Stim and NoStim were the default-mode and frontoparietal network (Figure 5C), both spatially distant from the most common stimulation sites. These two networks harbour several integral brain hubs, often referred to as the brain's rich-club, with strong inter-region connectivity (van den Heuvel and Sporns, 2011). This provides further evidence that focal brain stimulation induces widespread network effects.

Replication across multiple network parameters and densities

We replicated our result of reduced network switching during Stim versus NoStim epochs (FDR corrected) for 16 γ/ω parameter combinations (γ = 1, 1.1, 1.2 and 1.3 and ω = 0.1, 1, 2 and 3). We also replicated our results across several proportionally thresholded network densities, preserving

10%, 15% and 20% of phase synchrony connection-pairs. Although all network densities were statistically significant between Stim and NoStim epochs (FDR corrected), there was a trend towards greater statistical power between Stim and NoStim epochs at a lower network density threshold with fewer network connections (Figure S5). Sparse networks may be advantageous in multilayer network models as they are less likely to contain spurious connections (Fornito et al., 2012).

Instantaneous phase synchrony is also decreased during brain stimulation

Lastly, we investigated whether the underlying instantaneous phase synchrony between brain regions –i.e., the input data to our multilayer modularity model– was also modulated by the effect of brain stimulation. We found that the coefficient of variation of instantaneous phase synchrony was reduced during Stim epochs compared to NoStim epochs (averaged across all brain regions and Stim/NoStim epochs – paired t-test: $t(159) = 10.7$, $p < 0.001$). The coefficient of variation was computed as the standard deviation of instantaneous phase synchrony divided by the mean of instantaneous phase synchrony (σ/μ), using a network density of 15%. In total, 81% (130/160) of rsMRI scans displayed reduced coefficient of variance of phase synchrony during intracranial brain stimulation, all with a negative gradient between NoStim and Stim epochs. In turn, reduced instantaneous phase synchrony may be a potential mechanism of attenuated network switching during brain stimulation (Figure S6).

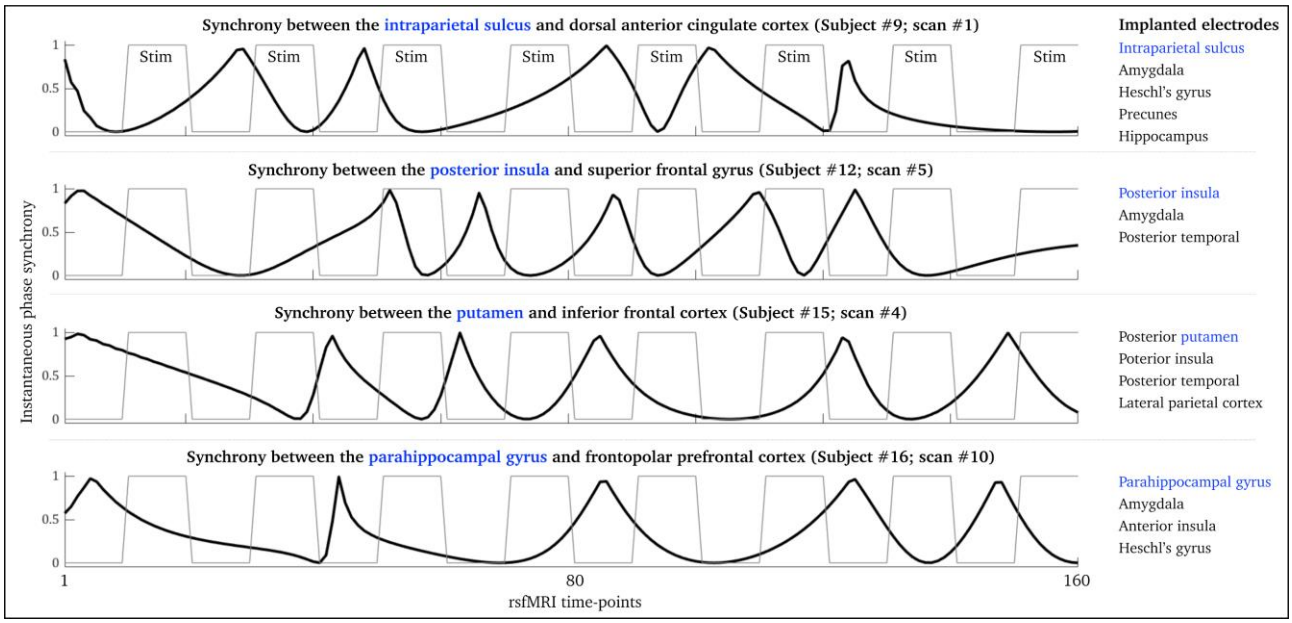

Figure 6: Examples of instantaneous phase synchrony time-series: *These four time-series each represent the synchrony between two brain regions for representative individuals. The blue colour highlight brain regions that harbour an intracranial electrode. The Spearman's ρ correlation between the instantaneous phase synchrony time-series and the block design (Stim/NoStim) was -0.48 (p<0.001 – first row), -0.51 (p<0.001 – second row), -0.47 (p<0.001 – third row) and -0.42 (p<0.001 – last row)*

In Figure 6 we present four time-series, each representing the instantaneous phase synchrony between two brain regions, where one brain region is located proximate to a stimulation site and the other brain region is distant from a stimulation site. These time-series show an inverse correlation between brain stimulation and instantaneous phase synchrony and highlights that distant network properties are associated with stimulation targets.

Discussion

We observed a reduction in brain network switching during intracranial brain stimulation (Figure 3A), which was stable across a range of network parameters (Figure S5). Intracranial stimulation affected widespread brain networks beyond the stimulation sites (Figure 5), likely reflecting a reduction in phase synchrony between brain regions during brain stimulation (Figure S6). This suggests that perturbation of the human brain is observable with rsfMRI network models and it is associated with widespread network changes. Our results validate multilayer network models as a potential tool to understand how the brain dynamically change over time and also how spatiotemporal brain properties are altered in neurological disease. From a clinical standpoint, our results suggest that stimulation-induced reduction of network switching can potentially normalize aberrant brain dynamics associated with disorders such as epilepsy (Pedersen et al, 2017).

Although the neuronal mechanisms of intracranial brain stimulation are complex, it is well established that invasive brain stimulation affects the cellular, electrical, molecular and network architecture of the brain (Jakobs et al., 2019). Network effects of brain stimulation (i.e., brain changes that occur distant to the stimulation target) are thought to be mediated by large and myelinated axons becoming depolarised and transformed into action potentials (Johnson et al., 2008). In line with our results, Alhourani et al. (2015) suggest that the underlying network mechanisms of intracranial brain stimulation represent a reduction of synchrony between remote brain regions that is achieved by perturbing afferent and efferent neurons that are (directly or indirectly) connected to the stimulation target. This is supported by Middlebrooks et al. (2018) who showed that epilepsy individuals who had a positive clinical response to brain stimulation to the anterior thalamus displayed greater connectivity in the default-mode network, compared to patients who did not respond positively to brain stimulation. This reinforces that brain stimulation impacts widespread brain networks beyond the stimulation target.

Invasive brain stimulation has Class I evidence for seizure reduction in treatment-resistant epilepsy (Li and Cook, 2018), from randomised controlled trials with two different stimulation targets (Fisher et al., 2010; Morrell and RNS System in Epilepsy Study Group, 2011). Brain networks may normalise during invasive brain stimulation and attenuated network switching may represent a putative marker

of therapeutic normalisation. This fits the clinical pattern of epilepsy, given that increased rsfMRI brain connectivity is a common trait in people with treatment-resistant focal epilepsy (Pedersen et al., 2015). Similarly, people with Parkinson's disease undergo a normalisation of functional connectivity similar to healthy controls, during brain stimulation of the subthalamic nucleus (Horn et al., 2019). In combination with our findings, these studies suggest that novel network models may be used to inform the efficacy of brain stimulation in a range of neurological conditions (Halu et al., 2019).

The most common stimulation sites in this study were in the mesial temporal lobes (and especially the amygdala) but decreased network switching during intracranial stimulation was predominantly observed in the spatially distant default-mode and frontoparietal networks. In total, less than 40% of intracranial electrodes overlapped with statistically significant brain regions with reduced network switching during brain stimulation (Figure 5B). Brain stimulation is unlikely to only affect rsfMRI network properties that are distant from the stimulation sites. There are two plausible explanations of why we did not observe a statistically significant reduction in network switching in all the stimulation sites. The first explanation is based on our group-level research design. Electrode locations varied markedly between participants in this study (even within the amygdala), and rsfMRI effects from individual stimulation sites may cancel out within a group-level statistical test. Future studies will benefit from investigating brain regions associated with individual-level network switching during intracranial brain stimulation. For example, what network properties are affected by specific cortical or sub-cortical stimulation sites in individual subjects, and what is their relationship with individual clinical symptomatology and treatment efficacy? The second explanation is that spatial distortion induced by the intracranial electrodes attenuate the fMRI signal near the stimulation sites (Lee et al., 2012). We are encouraged by recent advances in the field demonstrating that graphene fibre electrodes reduce MRI distortion proximate to the stimulation site (Zhao et al., 2020). Graphene fibre electrodes will benefit future rsfMRI and brain stimulation studies as we seek to further understand local and global brain network variability in response to intracranial brain stimulation.

Another limitation of this study is the relatively short duration of the rsfMRI scans (9 minutes). This precluded testing of the long-lasting network effects of intracranial brain stimulation. However, we observed a sudden drop in brain network switching in the early epochs of the rsfMRI scans, followed by a plateau in brain network switching, suggesting that the initial effects of brain stimulation may persist for at least 10 minutes (Fig. 4). Longer rsfMRI scans are needed to clarify the duration of stimulation-induced brain network effects A longer period of rsfMRI recording before the onset of the first brain stimulation (here, ~30 seconds into the scan) is also beneficial to ensure the participants are settled and relaxed before the onset of brain stimulation, and it would allow for improved control of filter-related issues that can occur at the start/end of rsfMRI signals.

Our results suggest that large-scale networks are dynamically modulated by neuronal perturbation induced by intracranial brain stimulation, affecting brain regions and networks distant from the stimulation target. We believe that this research is a necessary first step to enable further investigation into subject-specific network changes following intracranial brain stimulation, as this may aid the clinical decision support of refractory neurological diseases.

Methods

Participants

We downloaded 160 rsfMRI datasets from 26 people with epilepsy from openneuro.org (https://openneuro.org/datasets/ds002799/versions/1.0.3). The dataset is described in detail in Oya et al. (2017) and Thompson et al. (2020).

Data and code availability

Open-access MATLAB-based scripts for computing instantaneous phase synchrony, multilayer modularity and network switching can be found at https://github.com/MangorPedersen/fMRI_codes/.

rsfMRI and brain stimulation parameters

The length of each rsfMRI scan varied between participants. We included rsfMRI scans that were more than 9 minutes long (160 scans in total). The rsfMRI echo time (TE) was 30 milliseconds, and the data had a voxel size of 3×3×3 millimetre. There was no significant difference in head motion between NoStim and Stim epochs (Thompson et al., 2020). The repetition time (TR) of the rsfMRI data was 3000 milliseconds with a delay in TR of 100 milliseconds. The electrical stimulation was delivered during this TR delay and ensured no artefacts between MRI radiofrequency coils and electrodes (Oya et al., 2017). The brain stimulation consisted of bi-phasic charge-balanced square pulses (50-90 milliseconds in length, 8-12 milliamps, and 5-9 pulses at a 100 Hz stimulation rate).

Results included in this manuscript come from pre-processing performed using fMRIPrep 1.5.1rc1 (RRID: SCR_016216 - Esteban et al., 2019, 2020), which is based on Nipype 1.3.0-rc1 (RRID: SCR_002502 - Gorgolewski et al., 2011).

Anatomical MRI pre-processing

The T1-weighted (T1w) image was corrected for intensity non-uniformity (INU) with N4BiasFieldCorrection (Tustison et al., 2010), distributed with ANTs 2.2.0 (RRID: SCR_004757) (Avants et al., 2008), and used as T1w-reference throughout the workflow. The T1w-reference was then skull-stripped with a Nipype implementation of the antsBrainExtraction.sh workflow (from ANTs), using OASIS30ANTs as a target template. Brain tissue segmentation of cerebrospinal fluid

(CSF), white matter (WM) and grey matter (GM) were performed on the brain extracted T1w using fast (FSL 5.0.9, RRID: SCR_002823 - Zhang et al., 2001). Brain surfaces were reconstructed using recon-all (FreeSurfer 6.0.1, RRID: SCR_001847 - Dale et al., 1999), and the brain mask estimated previously was refined with a custom variation of the method to reconcile ANTs-derived and FreeSurfer-derived segmentation of the cortical grey-matter of Mindboggle (RRID: SCR_002438 - Klein et al., 2017).

Volume-based spatial normalization to one standard space (MNI152NLin2009cAsym) was performed through nonlinear registration with antsRegistration (ANTs 2.2.0), using brain-extracted versions of both T1w reference and the T1w template. The following template was selected for spatial normalization: ICBM 152 Nonlinear Asymmetrical template version 2009c (RRID:SCR_008796; TemplateFlow ID: [MNI152NLin2009cAsym] - Fonov et al., 2009).

rsfMRI pre-processing

For each of the BOLD runs found per subject (across all tasks and sessions), the following pre-processing was performed. First, a reference volume and its skull-stripped version were generated using a custom methodology of fMRIPrep. A deformation field to correct for susceptibility distortions was estimated based on fMRIPrep's field map-less approach. The deformation field is that resulting from co-registering the BOLD reference to the same-subject T1w-reference with its intensity inverted (Huntenburg, 2014; Wang et al., 2017). Registration was performed with antsRegistration (ANTs 2.2.0), and the process regularized by constraining deformation to be nonzero only along the phase-encoding direction and modulated with an average field map template (Treiber et al., 2016). Based on the estimated susceptibility distortion, an unwarped BOLD reference was calculated for a more accurate co-registration with the anatomical reference. The BOLD reference was then co-registered to the T1w reference using bbregister (FreeSurfer) which implements boundary-based registration (Greve and Fischl, 2009). Co-registration was configured with six degrees of freedom.

Head-motion parameters for the BOLD reference (transformation matrices, and six corresponding rotation and translation parameters) were estimated before any spatiotemporal filtering using mcflirt (FSL 5.0.9) (Jenkinson et al., 2002). BOLD runs were slice-time corrected using 3dTshift from AFNI 20160207 (RRID: SCR_005927 - Cox and Hyde, 1997). The BOLD time-series were resampled to surfaces on the following spaces: fsnative, fsaverage5. The BOLD time-series (including slice-timing correction when applied) were resampled onto their original, native space by applying a single, composite transform to correct for head-motion and susceptibility distortions. These resampled BOLD time-series will be referred to as pre-processed BOLD in original space, or just pre-processed BOLD. The BOLD time-series were resampled into standard space, generating a pre-processed

BOLD run in ['MNI152NLin2009cAsym'] space. First, a reference volume and its skull-stripped version were generated using a custom methodology of fMRIPrep. Several confounding time-series were calculated based on the pre-processed BOLD: framewise displacement (FD), DVARS and three region-wise global signals. FD and DVARS are calculated for each functional run, both using their implementations in Nipype (following the definitions in Power et al., 2014). The three global signals are extracted within the CSF, the WM, and the whole-brain masks. Additionally, a set of physiological regressors were extracted to allow for component-based noise correction (CompCor) (Behzadi et al., 2007). Principal components are estimated after high-pass filtering the pre-processed BOLD time-series (using a discrete cosine filter with 128-second cut-off) for the two CompCor variants: temporal (tCompCor) and anatomical (aCompCor). tCompCor components are then calculated from the top 5% variable voxels within a mask covering the subcortical regions. This subcortical mask is obtained by heavily eroding the brain mask, which ensures it does not include cortical GM regions.

For aCompCor, components are calculated within the intersection of the aforementioned mask and the union of CSF and WM masks calculated in T1w space, after their projection to the native space of each functional run (using the inverse BOLD-to-T1w transformation). Components are also calculated separately within the WM and CSF masks. For each CompCor decomposition, the k components with the largest singular values are retained, such that the retained components' time-series are sufficient to explain 50 percent of variance across the nuisance mask (CSF, WM, combined, or temporal). The remaining components are dropped from consideration. The head-motion estimates calculated in the correction step were also placed within the corresponding confounds file. The confound time-series derived from head motion estimates and global signals were expanded with the inclusion of temporal derivatives and quadratic terms for each (Satterthwaite et al., 2013). Frames that exceeded a threshold of 0.5 mm FD or 1.5 standardised DVARS were annotated as motion outliers. All resamplings can be performed with a single interpolation step by composing all the pertinent transformations (i.e. head-motion transform matrices, susceptibility distortion correction, and co-registrations to anatomical and output spaces). Gridded (volumetric) resamplings were performed using antsApplyTransforms (ANTs), configured with Lanczos interpolation to minimize the smoothing effects of other kernels (Lanczos, 1964).

Many internal operations of fMRIPrep use Nilearn 0.5.2 (RRID: SCR_001362 - Abraham et al., 2014), mostly within the functional processing workflow. For more details of the pipeline, see the section corresponding to workflows in fMRIPrep's documentation (https://fmriprep.org//downloads/en/0.2.0/pdf/).

Filtering and parcellation of rsfMRI data

The rsfMRI data was zero-phase filtered within narrow-band frequencies of 0.03 and 0.07 Hz, using a 5th order Butterworth filter (‘*filtfilt’* function in MATLAB). After filtering the rsfMRI in the forward direction, we also filtered the data in the reverse order to minimise distortion and filter effects at the beginning and end of the signals (Dwivedi and Vyas, 2011). Narrow-band filtering is a requirement of instantaneous phase synchrony, to satisfy the Bedrossian’s theorem when using the Hilbert transform for time-series analyses (Honari et al., 2020).

The average fMRI signal within 196 brain regions was extracted for analysis. We combined the cortical parcellation mask the Human Connectome Project (Glasser et al., 2016) with 180 bilateral cortical regions and the sub-cortical parcellation mask from Tian et al. (2020b) with 16 bilateral sub-cortical regions. We used a symmetric brain parcellation mask –i.e., the same parcel in homologous brain regions– to counter the laterality effects of temporal lobe epilepsy where seizures predominantly originate from a single hemisphere (Adcock et al., 2003). For each rsfMRI scan, this results in a 3D tensor of size 196 x 196 x 160 that represents the interconnectivity between each of the 196 brain regions, for 160 rsfMRI time-points (80 Stim time-points and 80 NoStim time-points, partitioned into alternating epochs each containing 10 time-points – see Figure 2).

Instantaneous Phase Synchrony

Instantaneous phase synchrony is calculated by using the Hilbert transform (Bedrosian, 1963) to extract phase information between all brain regions (see Figure S7). In the equation below, Y is a 2D matrix comprising the average narrow-band rsfMRI data across 196 brain regions and 160 time-points, using the same procedure as reported in Glerean et al. (2012); Pedersen et al. (2018b); and Ponce-Alvarez et al. (2015). $z_{m_1}[t]$ and $z_{m_2}[t]$ is the analytic representations of the rows in Y ($y_{m_1}[t]$ and $y_{m_2}[t]$):

$$z_{m_1}[t] = y_{m_1}[t] + j\tilde{y}_{m_1}[t] = a_{m_1}[t]e^{j\varphi_{m_1}[t]}$$

$$z_{m_2}[t] = y_{m_2}[t] + j\tilde{y}_{m_2}[t] = a_{m_2}[t]e^{j\varphi_{m_2}[t]}.$$

Here, $j = \sqrt{-1}$, $\tilde{y}$ represents the Hilbert transformation of y where $a_{m_1}[t]$ ad $a_{m_2}[t]$ is the instantaneous amplitudes. $\varphi_{m_1}[t]$ and $\varphi_{m_2}[t]$ being the instantaneous phases of $y_{m_1}[t]$ and $y_{m_2}[t]$, respectively. $y_{m_1}[t]$ and $y_{m_2}[t]$ are phase-locked if:

$$\left|\varphi_{m_1}[t] - \varphi_{m_2}[t]\right| \approx 0,$$

with $|.|$ as an absolute value operator. The instantaneous phase difference between $\varphi_{m_1}[t]$ and $\varphi_{m_2}[t]$ is derived from the rows in the analytic matrix Z.

$$IPS_{m_1,m_2}[t] = \text{abs}(\sin(\varphi_{m_1}[t] - \varphi_{m_2}[t])).$$

The angle information between signals allows us to quantify their phase synchrony by estimating the absolute sinusoid difference between the signals, at each time-point, t. We then computed 1 minus phase synchrony ($1 - IPS$) to obtain a numerical range of phase coherence between 0 and 1. A value of 0 indicates no phase synchrony between two brain regions, and a value of 1 indicates that two brain regions are fully synchronous (Mormann et al., 2000).

It remains debated what sparsity level matrices contain optimal levels of biological information and a minimal influence of noise confounders (Fornito et al., 2012; van den Heuvel et al., 2017; Langer et al., 2013). To minimise potential confounders in this study, we thresholded and binarized matrices at several density thresholds, retaining 10%, 15%, and 20% of the strongest instantaneous phase synchrony connection-pairs. In Figure S8, we provide the minimum phase synchrony values (i.e., threshold cut-off values) for each of these thresholds.

Multilayer modularity and network switching rate

To quantify the rate of brain network switching we first generated a multilayer modularity model (Mucha et al., 2010). The multilayer modularity model is based on the Louvain modularity algorithm (Blondel et al., 2008; Lancichinetti and Fortunato, 2012):

$$Q(\gamma, \omega) = \frac{1}{2\mu} \sum_{ijrt} \left[\left((A_{ijr} - \gamma_r \frac{k_{ir} k_{jr}}{2m_r}) \delta(M_{ir}, M_{jr}) + \delta(i,j) \times \omega_{jtr} \right] \delta(M_{ir}, M_{jt}) \right.$$

The input to the multilayer modularity model is A and denote the thresholded and binarized 3D instantaneous phase synchrony tensors, for each rsfMRI scan. A_{ijr} is the phase synchronisation between brain region, i and j, for time-point r. k is the degree (the total number of connections) at brain region i at time-point r, and m refers to the total degree across the 196 brain regions at timepoint r. The Newman-Girvan null model of intra-network connectivity ($2m_r$) is used to quantify whether the intramodular degree is greater than expected by chance (Sarzynska et al., 2016). Topological modularity is controlled by the network resolution parameter, γ_r, at time-point r. We used γ = 1, 1.1, 1.2 and 1.3 in this study where low γ values will return larger and fewer brain modules whereas high γ values will return smaller and more brain modules. Temporal connectivity is controlled by the coupling parameter, ω_{jtr}, at brain region j between adjacent layers (i.e., adjacent time-points) r and

t. We used ω temporal coupling parameters of 0.1, 1, 2 and 3 (in line with recommendations from Yang et al., 2020).

$\delta(M_{ir}, M_{jr})$ and $\delta(M_{ir}, M_{jt})$ has a value of 1 if two brain regions of interest (i, j) are located within the same module, and 0 if they are allocated to two separate modules (Bassett et al., 2013). Modularity maximisation methods are inherently heuristic (Good et al., 2010), and our multilayer modularity models converged after an average of 4 iterations across all rsfMRI scans. The modular decomposition across all participants is displayed in Figure S9 and the most common modules that resembled i) the visual network, ii) the somatomotor network, iii) the frontoparietal network, iv) the default-mode network and v) sub-cortical brain regions. The average network modularity was calculated with the Q-value, which range between 0 connections (no modular structure and between-module connectivity) to 1 (fully modular structure and within-module connectivity). Q-values and number of modules for all network densities (10%, 15% and 20%) as well as γ (γ = 1, 1.1, 1.2, and 1.3) and ω (ω = 0.1, 1, 2, 3) values are found in Figure S10.

The network switching rate is derived from the multilayer modularity model and can be written as:

$$S = \frac{1}{N}\sum_{i}^{N} s_i,$$

where s_i is the network switching at node i, calculated as the number of times a brain region transits between network modules, divided by the total number of possible network transitions (Bassett et al., 2011).

Statistical analysis

As reported in Figure 3, we used one-way within-subjects (repeated measures) ANOVA to infer statistical differences between all eight Stim epochs and eight NoStim epochs (120 Stim/NoStim epoch combinations in total). Post-hoc comparisons between all possible epochs were computed with Bonferroni correction with a critical probability value of $p < 0.05$. We used a univariate paired-samples t-test to infer statistical differences in network switching for 196 brain regions between the mean of all Stim and NoStim epochs. We used FDR correction at $q < 0.05$ (Benjamini and Hochberg, 1995) to control for multiple comparisons across all brain regions (Figure 5A).

Acknowledgements

We thank the researchers from the University of Iowa comprehensive epilepsy program (Department of Neurosurgery), as well as their collaborators listed in Oya et al. (2017) and Thompson et al. (2020) for acquiring and freely releasing this dataset. The authors declare no competing interests.

References

Abraham, A., Pedregosa, F., Eickenberg, M., Gervais, P., Mueller, A., Kossaifi, J., Gramfort, A., Thirion, B., and Varoquaux, G. (2014). Machine learning for neuroimaging with scikit-learn. Front. Neuroinformatics *8*.

Adcock, J.E., Wise, R.G., Oxbury, J.M., Oxbury, S.M., and Matthews, P.M. (2003). Quantitative fMRI assessment of the differences in lateralization of language-related brain activation in patients with temporal lobe epilepsy. NeuroImage *18*, 423–438.

Alhourani, A., McDowell, M.M., Randazzo, M.J., Wozny, T.A., Kondylis, E.D., Lipski, W.J., Beck, S., Karp, J.F., Ghuman, A.S., and Richardson, R.M. (2015). Network effects of deep brain stimulation. J. Neurophysiol. *114*, 2105–2117.

Avants, B.B., Epstein, C.L., Grossman, M., and Gee, J.C. (2008). Symmetric diffeomorphic image registration with cross-correlation: Evaluating automated labeling of elderly and neurodegenerative brain. Med. Image Anal. *12*, 26–41.

Bassett, D.S., Wymbs, N.F., Porter, M.A., Mucha, P.J., Carlson, J.M., and Grafton, S.T. (2011). Dynamic reconfiguration of human brain networks during learning. Proc. Natl. Acad. Sci. U. S. A. *108*, 7641–7646.

Bassett, D.S., Porter, M.A., Wymbs, N.F., Grafton, S.T., Carlson, J.M., and Mucha, P.J. (2013). Robust detection of dynamic community structure in networks. Chaos Woodbury N *23*, 013142.

Bedrosian, E. (1963). A product theorem for Hilbert transforms. Proc. IEEE *51*, 868–869.

Behzadi, Y., Restom, K., Liau, J., and Liu, T.T. (2007). A component based noise correction method (CompCor) for BOLD and perfusion based fMRI. NeuroImage *37*, 90–101.

Benjamini, Y., and Hochberg, Y. (1995). Controlling the False Discovery Rate: A Practical and Powerful Approach to Multiple Testing. J. R. Stat. Soc. Ser. B Methodol. *57*, 289–300.

Bernhardt, B.C., Chen, Z., He, Y., Evans, A.C., and Bernasconi, N. (2011). Graph-Theoretical Analysis Reveals Disrupted Small-World Organization of Cortical Thickness Correlation Networks in Temporal Lobe Epilepsy. Cereb. Cortex bhq291.

Bernhardt, B.C., Hong, S.-J., Bernasconi, A., and Bernasconi, N. (2015). Magnetic resonance imaging pattern learning in temporal lobe epilepsy: classification and prognostics. Ann. Neurol. *77*, 436–446.

Betzel, R.F., and Bassett, D.S. (2017). Multi-scale brain networks. NeuroImage *160*, 73–83.

Betzel, R.F., Satterthwaite, T.D., Gold, J.I., and Bassett, D.S. (2017). Positive affect, surprise, and fatigue are correlates of network flexibility. Sci. Rep. *7*, 520.

Blondel, V.D., Guillaume, J.-L., Lambiotte, R., and Lefebvre, E. (2008). Fast unfolding of communities in large networks. J. Stat. Mech. Theory Exp. *2008*, P10008.

Braun, U., Schäfer, A., Walter, H., Erk, S., Romanczuk-Seiferth, N., Haddad, L., Schweiger, J.I., Grimm, O., Heinz, A., Tost, H., et al. (2015). Dynamic reconfiguration of frontal brain networks during executive cognition in humans. Proc. Natl. Acad. Sci. U. S. A. *112*, 11678–11683.

Cox, R.W., and Hyde, J.S. (1997). Software tools for analysis and visualization of fMRI data. NMR Biomed. *10*, 171–178.

Dale, A.M., Fischl, B., and Sereno, M.I. (1999). Cortical Surface-Based Analysis: I. Segmentation and Surface Reconstruction. NeuroImage *9*, 179–194.

De Domenico, M. (2017). Multilayer modeling and analysis of human brain networks. GigaScience *6*, 1–8.

Dwivedi, A.K., and Vyas, O.P. (2011). An Exploratory Study of Experimental Tools for Wireless Sensor Networks. Wirel. Sens. Netw. *03*, 215–240.

Esteban, O., Markiewicz, C.J., Blair, R.W., Moodie, C.A., Isik, A.I., Erramuzpe, A., Kent, J.D., Goncalves, M., DuPre, E., Snyder, M., et al. (2019). fMRIPrep: a robust preprocessing pipeline for functional MRI. Nat. Methods *16*, 111–116.

Esteban, O., Markiewicz, C.J., Goncalves, M., DuPre, E., Kent, J.D., Salo, T., Ciric, R., Pinsard, B., Blair, R.W., Poldrack, R.A., et al. (2020). fMRIPrep: a robust preprocessing pipeline for functional MRI (Zenodo).

Finc, K., Bonna, K., He, X., Lydon-Staley, D.M., Kühn, S., Duch, W., and Bassett, D.S. (2020). Dynamic reconfiguration of functional brain networks during working memory training. Nat. Commun. *11*, 2435.

Fisher, R., Salanova, V., Witt, T., Worth, R., Henry, T., Gross, R., Oommen, K., Osorio, I., Nazzaro, J., Labar, D., et al. (2010). Electrical stimulation of the anterior nucleus of thalamus for treatment of refractory epilepsy. Epilepsia *51*, 899–908.

Fonov, V., Evans, A., McKinstry, R., Almli, C., and Collins, D. (2009). Unbiased nonlinear average age-appropriate brain templates from birth to adulthood. NeuroImage *47*, S102.

Fornito, A., Zalesky, A., Pantelis, C., and Bullmore, E.T. (2012). Schizophrenia, neuroimaging and connectomics. NeuroImage *62*, 2296–2314.

Garcia, L., D'Alessandro, G., Bioulac, B., and Hammond, C. (2005). High-frequency stimulation in Parkinson's disease: more or less? Trends Neurosci. *28*, 209–216.

Gerraty, R.T., Davidow, J.Y., Foerde, K., Galvan, A., Bassett, D.S., and Shohamy, D. (2018). Dynamic Flexibility in Striatal-Cortical Circuits Supports Reinforcement Learning. J. Neurosci. *38*, 2442–2453.

Gifford, G., Crossley, N., Kempton, M.J., Morgan, S., Dazzan, P., Young, J., and McGuire, P. (2020). Resting state fMRI based multilayer network configuration in patients with schizophrenia. NeuroImage Clin. *25*, 102169.

Glasser, M.F., Coalson, T.S., Robinson, E.C., Hacker, C.D., Harwell, J., Yacoub, E., Ugurbil, K., Andersson, J., Beckmann, C.F., Jenkinson, M., et al. (2016). A multi-modal parcellation of human cerebral cortex. Nature *536*, 171–178.

Glerean, E., Salmi, J., Lahnakoski, J.M., Jaaskelainen, I.P., and Sams, M. (2012). Functional Magnetic Resonance Imaging Phase Synchronization as a Measure of Dynamic Functional Connectivity. Brain Connect. *2*, 91–101.

Good, B.H., de Montjoye, Y.-A., and Clauset, A. (2010). Performance of modularity maximization in practical contexts. Phys. Rev. E *81*, 046106.

Gorgolewski, K., Burns, C.D., Madison, C., Clark, D., Halchenko, Y.O., Waskom, M.L., and Ghosh, S.S. (2011). Nipype: A Flexible, Lightweight and Extensible Neuroimaging Data Processing Framework in Python. Front. Neuroinformatics *5*.

Greve, D.N., and Fischl, B. (2009). Accurate and robust brain image alignment using boundary-based registration. NeuroImage *48*, 63–72.

Gummadavelli, A., Kundishora, A.J., Willie, J.T., Andrews, J.P., Gerrard, J.L., Spencer, D.D., and Blumenfeld, H. (2015). Neurostimulation to improve level of consciousness in patients with epilepsy. Neurosurg. Focus *38*, E10.

Halu, A., De Domenico, M., Arenas, A., and Sharma, A. (2019). The multiplex network of human diseases. Npj Syst. Biol. Appl. *5*, 1–12.

Harlalka, V., Bapi, R.S., Vinod, P.K., and Roy, D. (2019). Atypical Flexibility in Dynamic Functional Connectivity Quantifies the Severity in Autism Spectrum Disorder. Front. Hum. Neurosci. *13*, 6.

van den Heuvel, M.P., and Sporns, O. (2011). Rich-Club Organization of the Human Connectome. J. Neurosci. *31*, 15775–15786.

van den Heuvel, M.P., de Lange, S.C., Zalesky, A., Seguin, C., Yeo, B.T.T., and Schmidt, R. (2017). Proportional thresholding in resting-state fMRI functional connectivity networks and consequences for patient-control connectome studies: Issues and recommendations. NeuroImage *152*, 437–449.

Honari, H., Choe, A.S., and Lindquist, M.A. (2020). Evaluating phase synchronization methods in fMRI: a comparison study and new approaches. NeuroImage, *228*, 117704.

Hong, S.-J., Bernhardt, B.C., Caldairou, B., Hall, J.A., Guiot, M.C., Schrader, D., Bernasconi, N., and Bernasconi, A. (2017). Multimodal MRI profiling of focal cortical dysplasia type II. Neurology *88*, 734–742.

Horn, A., Wenzel, G., Irmen, F., Huebl, J., Li, N., Neumann, W.-J., Krause, P., Bohner, G., Scheel, M., and Kühn, A.A. (2019). Deep brain stimulation induced normalization of the human functional connectome in Parkinson's disease. Brain *142*, 3129–3143.

Huntenburg, J.M. (2014). Evaluating nonlinear coregistration of BOLD EPI and T1w images. Freie Universität Berlin.

Jakobs, M., Fomenko, A., Lozano, A.M., and Kiening, K.L. (2019). Cellular, molecular, and clinical mechanisms of action of deep brain stimulation-a systematic review on established indications and outlook on future developments. EMBO Mol. Med. *11*.

Jenkinson, M., Bannister, P., Brady, M., and Smith, S. (2002). Improved Optimization for the Robust and Accurate Linear Registration and Motion Correction of Brain Images. NeuroImage *17*, 825–841.

Johnson, M.D., Miocinovic, S., McIntyre, C.C., and Vitek, J.L. (2008). Mechanisms and targets of deep brain stimulation in movement disorders. Neurotherapeutics *5*, 294–308.

Khan, S., Wright, I., Javed, S., Sharples, P., Jardine, P., Carter, M., and Gill, S.S. (2009). High frequency stimulation of the mamillothalamic tract for the treatment of resistant seizures associated with hypothalamic hamartoma. Epilepsia *50*, 1608–1611.

Klein, A., Ghosh, S.S., Bao, F.S., Giard, J., Häme, Y., Stavsky, E., Lee, N., Rossa, B., Reuter, M., Neto, E.C., et al. (2017). Mindboggling morphometry of human brains. PLOS Comput. Biol. *13*, e1005350.

Lafreniere-Roula, M., Kim, E., Hutchison, W.D., Lozano, A.M., Hodaie, M., and Dostrovsky, J.O. (2010). High-frequency microstimulation in human globus pallidus and substantia nigra. Exp. Brain Res. *205*, 251–261.

Lancichinetti, A., and Fortunato, S. (2012). Consensus clustering in complex networks. Sci. Rep. *2*, 336.

Lanczos, C. (1964). Evaluation of Noisy Data. J. Soc. Ind. Appl. Math. Ser. B Numer. Anal. *1*, 76–85.

Langer, N., Pedroni, A., and Jäncke, L. (2013). The Problem of Thresholding in Small-World Network Analysis. PLoS ONE *8*, e53199.

Lee, K.J., Shon, Y.M., and Cho, C.B. (2012). Long-term outcome of anterior thalamic nucleus stimulation for intractable epilepsy. Stereotact. Funct. Neurosurg. *90*, 379–385.

Li, D.-H., and Yang, X.-F. (2017). Remote modulation of network excitability during deep brain stimulation for epilepsy. Seizure *47*, 42–50.

Li, M.C.H., and Cook, M.J. (2018). Deep brain stimulation for drug-resistant epilepsy. Epilepsia *59*, 273–290.

Li, Q., Wang, X., Wang, S., Xie, Y., Li, X., Xie, Y., and Li, S. (2019). Dynamic reconfiguration of the functional brain network after musical training in young adults. Brain Struct. Funct. *224*, 1781–1795.

Long, Y., Chen, C., Deng, M., Huang, X., Tan, W., Zhang, L., Fan, Z., and Liu, Z. (2019). Psychological resilience negatively correlates with resting-state brain network flexibility in young healthy adults: a dynamic functional magnetic resonance imaging study. Ann. Transl. Med. *7*.

Lydon-Staley, D.M., Ciric, R., Satterthwaite, T.D., and Bassett, D.S. (2018). Evaluation of confound regression strategies for the mitigation of micromovement artifact in studies of dynamic resting-state functional connectivity and multilayer network modularity. Netw. Neurosci. *3*, 427–454.

Middlebrooks, E.H., Grewal, S.S., Stead, M., Lundstrom, B.N., Worrell, G.A., and Van Gompel, J.J. (2018). Differences in functional connectivity profiles as a predictor of response to anterior thalamic nucleus deep brain stimulation for epilepsy: a hypothesis for the mechanism of action and a potential biomarker for outcomes. Neurosurg. Focus *45*, E7.

Mormann, F., Lehnertz, K., David, P., and E. Elger, C. (2000). Mean phase coherence as a measure for phase synchronization and its application to the EEG of epilepsy patients. Phys. Nonlinear Phenom. *144*, 358–369.

Morrell, M.J., and RNS System in Epilepsy Study Group (2011). Responsive cortical stimulation for the treatment of medically intractable partial epilepsy. Neurology *77*, 1295–1304.

Mucha, P.J., Richardson, T., Macon, K., Porter, M.A., and Onnela, J.-P. (2010). Community structure in time-dependent, multiscale, and multiplex networks. Science *328*, 876–878.

Oya, H., Howard, M.A., Magnotta, V.A., Kruger, A., Griffiths, T.D., Lemieux, L., Carmichael, D.W., Petkov, C.I., Kawasaki, H., Kovach, C.K., et al. (2017). Mapping effective connectivity in the human brain with concurrent intracranial electrical stimulation and BOLD-fMRI. J. Neurosci. Methods *277*, 101–112.

Paban, V., Modolo, J., Mheich, A., and Hassan, M. (2019). Psychological resilience correlates with EEG source-space brain network flexibility. Netw. Neurosci. *3*, 539–550.

Pedersen, M., Omidvarnia, A.H., Walz, J.M., and Jackson, G.D. (2015). Increased segregation of brain networks in focal epilepsy: An fMRI graph theory finding. NeuroImage Clin. *8*, 536–542.

Pedersen, M., Curwood, E.K., Vaughan, D.N., Omidvarnia, A.H., and Jackson, G.D. (2016). Abnormal Brain Areas Common to the Focal Epilepsies: Multivariate Pattern Analysis of fMRI. Brain Connect. *6*, 208–215.

Pedersen, M., Omidvarnia, A., Curwood, E.K., Walz, J.M., Rayner, G., and Jackson, G.D. (2017). The dynamics of functional connectivity in neocortical focal epilepsy. NeuroImage Clin. *15*, 209–214.

Pedersen, M., Zalesky, A., Omidvarnia, A., and Jackson, G.D. (2018a). Multilayer network switching rate predicts brain performance. Proc. Natl. Acad. Sci. *115*, 13376–13381.

Pedersen, M., Omidvarnia, A., Zalesky, A., and Jackson, G.D. (2018b). On the relationship between instantaneous phase synchrony and correlation-based sliding windows for time-resolved fMRI connectivity analysis. NeuroImage *181*, 85–94.

Ponce-Alvarez, A., Deco, G., Hagmann, P., Romani, G.L., Mantini, D., and Corbetta, M. (2015). Resting-State Temporal Synchronization Networks Emerge from Connectivity Topology and Heterogeneity. PLoS Comput Biol *11*, e1004100.

Power, J.D., Mitra, A., Laumann, T.O., Snyder, A.Z., Schlaggar, B.L., and Petersen, S.E. (2014). Methods to detect, characterize, and remove motion artifact in resting state fMRI. NeuroImage *84*, 320–341.

Sarzynska, M., Leicht, E.A., Chowell, G., and Porter, M.A. (2016). Null models for community detection in spatially embedded, temporal networks. J. Complex Netw. *4*, 363–406.

Satterthwaite, T.D., Elliott, M.A., Gerraty, R.T., Ruparel, K., Loughead, J., Calkins, M.E., Eickhoff, S.B., Hakonarson, H., Gur, R.C., Gur, R.E., et al. (2013). An improved framework for confound regression and filtering for control of motion artifact in the preprocessing of resting-state functional connectivity data. NeuroImage *64*, 240–256.

Schulze-Bonhage, A. (2017). Brain stimulation as a neuromodulatory epilepsy therapy. Seizure *44*, 169–175.

Shao, J., Dai, Z., Zhu, R., Wang, X., Tao, S., Bi, K., Tian, S., Wang, H., Sun, Y., Yao, Z., et al. (2019). Early identification of bipolar from unipolar depression before manic episode: Evidence from dynamic rfMRI. Bipolar Disord. *21*, 774–784.

Shine, J.M., Koyejo, O., and Poldrack, R.A. (2016). Temporal metastates are associated with differential patterns of time-resolved connectivity, network topology, and attention. Proc. Natl. Acad. Sci. *113*, 9888–9891.

Sporns, O., and Betzel, R.F. (2016). Modular Brain Networks. Annu. Rev. Psychol. *67*, 613–640.

Telesford, Q.K., Ashourvan, A., Wymbs, N.F., Grafton, S.T., Vettel, J.M., and Bassett, D.S. (2017). Cohesive network reconfiguration accompanies extended training. Hum. Brain Mapp. *38*, 4744–4759.

Thompson, W., Nair, R., Oya, H., Esteban, O., Shine, J., Petkov, C., Poldrack, R., Howard, M., and Adolphs, R. (2020). Human es-fMRI Resource: Concurrent deep-brain stimulation and whole-brain functional MRI. bioRxiv. doi: https://doi.org/10.1101/2020.05.18.102657.

Tian, S., Sun, Y., Shao, J., Zhang, S., Mo, Z., Liu, X., Wang, Q., Wang, L., Zhao, P., Chattun, M.R., et al. (2020a). Predicting escitalopram monotherapy response in depression: The role of anterior cingulate cortex. Hum. Brain Mapp. *41*, 1249–1260.

Tian, Y., Margulies, D.S., Breakspear, M., and Zalesky, A. (2020b). Topographic organization of the human subcortex unveiled with functional connectivity gradients. Nat. Neurosci. *23*, 1421–1432.

Toprani, S., and Durand, D.M. (2013). Long-lasting hyperpolarization underlies seizure reduction by low frequency deep brain electrical stimulation. J. Physiol. *591*, 5765–5790.

Treiber, J.M., White, N.S., Steed, T.C., Bartsch, H., Holland, D., Farid, N., McDonald, C.R., Carter, B.S., Dale, A.M., and Chen, C.C. (2016). Characterization and Correction of Geometric Distortions in 814 Diffusion Weighted Images. PLOS ONE *11*, e0152472.

Tustison, N.J., Avants, B.B., Cook, P.A., Zheng, Y., Egan, A., Yushkevich, P.A., and Gee, J.C. (2010). N4ITK: Improved N3 Bias Correction. IEEE Trans. Med. Imaging *29*, 1310–1320.

Vaiana, M., and Muldoon, S. (2018). Multilayer Brain Networks. J. Nonlinear Sci.

Wang, S., Peterson, D.J., Gatenby, J.C., Li, W., Grabowski, T.J., and Madhyastha, T.M. (2017). Evaluation of Field Map and Nonlinear Registration Methods for Correction of Susceptibility Artifacts in Diffusion MRI. Front. Neuroinformatics *11*.

Yang, Z., Telesford, Q.K., Franco, A.R., Lim, R., Gu, S., Xu, T., Ai, L., Castellanos, F.X., Yan, C.-G., Colcombe, S., et al. (2020). Measurement Reliability for Individual Differences in Multilayer Network Dynamics: Cautions and Considerations. NeuroImage 117489.

Yeo, B.T.T., Krienen, F.M., Sepulcre, J., Sabuncu, M.R., Lashkari, D., Hollinshead, M., Roffman, J.L., Smoller, J.W., Zöllei, L., Polimeni, J.R., et al. (2011). The organization of the human cerebral cortex estimated by intrinsic functional connectivity. J. Neurophysiol. *106*, 1125–1165.

Zangiabadi, N., Ladino, L.D., Sina, F., Orozco-Hernández, J.P., Carter, A., and Téllez-Zenteno, J.F. (2019). Deep Brain Stimulation and Drug-Resistant Epilepsy: A Review of the Literature. Front. Neurol. *10*.

Zhang, Y., Brady, M., and Smith, S. (2001). Segmentation of brain MR images through a hidden Markov random field model and the expectation-maximization algorithm. IEEE Trans. Med. Imaging *20*, 45–57.

Zhao, S., Li, G., Tong, C., Chen, W., Wang, P., Dai, J., Fu, X., Xu, Z., Liu, X., Lu, L., et al. (2020). Full activation pattern mapping by simultaneous deep brain stimulation and fMRI with graphene fiber electrodes. Nat. Commun. *11*, 1788.